A Multi-Scale Model for Ultra Short Pulsed Parallel Laser Structuring — Part I. the Micro-Scale Model

C. Heinigk*[1], T. Barthels[2], Dr. M. Nießen[2], and Prof. W. Schulz[2]

[1]Department NLD, RWTH Aachen University, Steinbachstr. 15, 52074 Aachen, Germany
[2]Fraunhofer ILT, Steinbachstr. 15, 52074 Aachen, Germany
*Corresponding author's e-mail: christian.heinigk@nld.rwth-aachen.de

In the field of consumer electronics, especially in display manufacturing, Full Metal Masks (FMMs) with ever increasing structural requirements are needed. In addition, manufacturing technologies should meet these requirements at high productivity. High power ultra short pulsed lasers in combination with a multi-beam scanner are a key enabler by combining the high precision of laser manufacturing tools with the productivity of parallel processing. In order to produce FMMs in the required quality, temperature-related distortions due to heat accumulation must be avoided. Therefore, a deep understanding of the process is essential. In this treatise, the ablation of a single hole by multiple laser pulses is modeled by three submodels: 1. a fluence threshold model, 2. a level-set method, and 3. a heat conduction problem. The simulation results are compared with experiments and show good agreement. A comprehensive simulation of a complete foil resolving each laser pulse is, however, not feasible because of the computational demands. In future research, a multi-scale model is developed which retains most of the accuracy while tremendously speeding up the computation to enable the simulation of the whole process.
DOI: 10.2961/jlmn.2021.02.2011
Keywords: ablation, ultra short pulsed laser structuring, laser fluence threshold, level set method, heat conduction

1. Introduction

In the field of consumer electronics FMMs with ever increasing structural requirements in display manufacturing are needed. Manufacturing technologies to meet high quality and productivity requirements are required. High power ultra short pulsed lasers in combination with a multi-beam scanner are flexible tools for high precision manufacturing [1]. FMMs can be produced structuring a thin INVAR foil which must be both temperature-stable and have high geometric processing requirements with an accuracy below 2 µm. Phenomena such as temperature-related distortion and discoloration due to heat accumulation must be avoided [2].

A deep understanding of the process is required to find suitable process parameters and to select appropriate processing strategies. To predict the ablation shape, temperature field and distortion in a multi-beam processing, the detailed simulation of the physical processes during and after the laser ablation is required. The structuring process will change the thermal and mechanical properties with each piece of material removed. The computation of a single bore hole shape is already very time consuming and requires computational resources such that the simulation of larger workpieces is out of reach. Therefore, a multiscale model is required involving the effects of all beamlets. Within this multi-scale model, a distinction is made between three different length and time scales which are referred to as micro-, meso-, and macro-scale, respectively.

On the micro-scale, structuring a single hole by multiple ultra short laser pulses is simulated. This is a free, moving boundary problem in which the ablation front is time dependent. In order to recover the evolving front, a level set method is used in which the Hamilton-Jacobi equation is solved [3]. A laser fluence threshold model has been implemented with which the ablation and the energy deposition per pulse are computed. Those parts of the laser fluence which do not contribute to the ablation heat the material [4]. From the solution to the heat-conduction problem, the thermal load and thermal induced stresses are computed.

On the meso-scale, a patch which consists of multiple laser structured holes laid out in a rectangular pattern is considered. In order to simulate such a patch, a Representative Volume Element (RVE) is defined based on the results of the single-hole-shape simulation. For each RVE, effective material properties are computed. These properties describe a homogenized material defined on a larger scale in which continuum assumptions can be made regarding the detailed behavior on the micro-scale.

Using this RVE, a thermo-elasto-plastic mechanical calculations can be performed on a higher length and time scale, which is referred to as the macro-scale. The macro-scale consists of multiple patches or even a whole FMM.

In this article, the focus is on the micro-scale model describing the layer-by-layer ablation of material by a guided laser focus along a predefined path with multiple passes. This article is structured as follows. First, the geometric setup is described in section 2. Then, the model is derived in section 3 and discretized in section 4. Section 5 shows an experimental validation of the simulation with an Ultra Short Pulse (USP) multi-beam scanner. A machining process with different properties considering both ablation and structuring is created, and the laser parameters are transferred to the simulation. The simulation results are in good agreement with the conducted experiments as discussed in section 6. Finally, a conclusion is drawn and future research directions

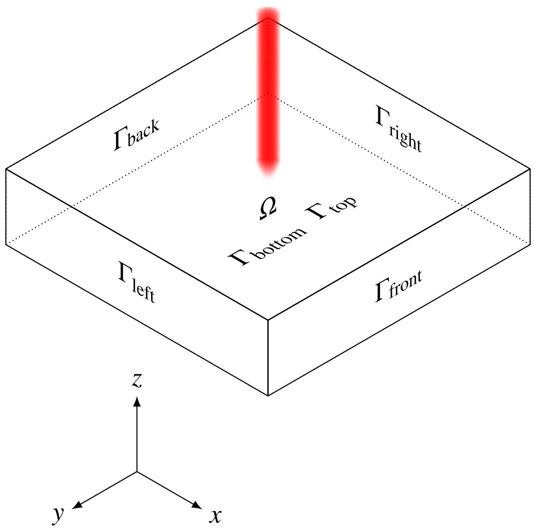

Fig. 1 The geometrical setup used throughout this treatise. The laser beam (red) hits a rectangular domain at the top face on which it is absorbed which leads to the ablation of material.

are highlighted (see section 7).

2. Geometrical Setup and Notation

Hereafter, a rectangular domain $\Omega \in \mathbb{R}^3$ is considered (cf. fig. 1). Whenever the time dependency is important, it shows in the notation with a subscript, i.e. Ω_t. Same holds for the boundary $\partial\Omega$. For a Neumann boundary Γ_N is written and for a Dirichlet boundary Γ_D. When both boundary conditions are considered, the boundary is split such that $\Omega = \Gamma_\mathrm{N} \cup \Gamma_\mathrm{D}$ and $\Gamma_\mathrm{N} \cap \Gamma_\mathrm{D} = \emptyset$. Note, that the boundary is time-dependent as an arbitrarily shaped bore hole is formed during processing, however, the dependency is not reflected in the notation. Without loss of generality, the time interval $\mathscr{I} := [0, t_\mathrm{end}]$ is considered. Furthermore, vector quantities are written with an arrow over a lower case character, e.g. $\vec{x}$, whereas matrix quantities are capitalized, e.g. $\vec{A}$. For entries, the arrow is dropped and index notation is used.

3. Modeling the Ablation of a Single Hole

The single hole ablation model consists of four steps. First, the absorbed fluence per pulse is computed and depending on a predefined threshold part of it drives the ablation and the rest diffuses into the material. From the amount of ablated material per pulse duration, a front velocity can be defined which enters a transport equation which in turn can be solved for the ablation front. The remaining fluence is considered a source in the heat conduction equation that models the heating of the material. Last but not least, knowing the temperature field within the material allows to define temperature induced strains which drive the plastic deformations in this process. In the following sections, the four steps are explained in more detail.

3.1. The Laser Fluence Threshold Model

Following the works of Jäggi et al. [5], Lauer, Jäggi, and Neuenschwander [6], Neuenschwander, Jaeggi, and Schmid [7], and Neuenschwander et al. [4], the ablation process is driven by the absorbed laser fluence. The absorbed fluence is a function of radius r and depth z, i.e. $F_\mathrm{abs}(r,z) : \mathbb{R} \times \mathbb{R} \to \mathbb{R}$. Given the laser fluence $F_\mathrm{L} : \mathbb{R} \to \mathbb{R}$, the reflectivity R, the penetration depth d_pen, and the angle of incidence θ, the absorbed fluence can be defined as

$$F_\mathrm{abs}(r,z) = (1-R)\cos(\theta) F_\mathrm{L}(r) e^{-\frac{z}{d_\mathrm{pen}}}. \tag{1}$$

Herein, the last first factor filters out the reflected parts, the second factor is understood as a projection of the incoming light at a possibly inclined surface, i.e. $\cos(\theta) = -\vec{s} \cdot \vec{n}$ with the Poynting vector $\vec{s}$ and the outward pointing unit normal $\vec{n}$. The last factor models how deep the fluence penetrates into the material.

Experiments show that material is ablated when the fluence reaches a certain threshold, i.e. $F_\mathrm{abs} \geq F_\mathrm{thr}$. In this case, an ablation depth can be derived from eq. (1) by solving $F_\mathrm{abs} = F_\mathrm{thr}$ for z, i.e.

$$z = d_\mathrm{pen} \ln \frac{(1-R) F_\mathrm{L}(r) \cos(\theta)}{F_\mathrm{thr}}. \tag{2}$$

This depth is, from now on, referred to as ablation depth $d_\mathrm{abl} = z$. Note, that the threshold fluence and, therefore, the ablation depth can be calibrated from experimental data.

For a Gaussian beam, the laser fluence $F_\mathrm{L}(r) : \mathbb{R} \to \mathbb{R}$ is defined as

$$F_\mathrm{L}(r) = F_0 e^{-2\frac{r^2}{\omega_0{}^2}}, \tag{3}$$

with the amplitude $F_0 = 2P_\mathrm{L}\tau_\mathrm{p}/(\pi\omega_0{}^2) = 2E_\mathrm{p}/(\pi\omega_0{}^2)$, the laser power P_L, pulse duration τ_p, pulse energy $E_\mathrm{p} = P_\mathrm{L}\tau_\mathrm{p}$, and beam waist ω_0.

So far polarization has not been accounted for. The reflection coefficients for perpendicularly polarized $(\cdot)_\perp$ and for parallel polarized $(\cdot)_\parallel$ light read

$$r_\perp = \left(\frac{E_\mathrm{0,r}}{E_\mathrm{0,i}}\right)_\perp = \frac{n_1\cos(\theta) - n_2\cos(\beta)}{n_1\cos(\theta) + n_2\cos(\beta)} \tag{4}$$

and

$$r_\parallel = \left(\frac{E_\mathrm{0,r}}{E_\mathrm{0,i}}\right)_\parallel = \frac{n_2\cos(\theta) - n_1\cos(\beta)}{n_2\cos(\theta) + n_1\cos(\beta)}, \tag{5}$$

respectively [8, chapter 14.2]. Herein, the reflective wave's complex amplitude $E_\mathrm{0,r}$ is compared to the incident wave's complex amplitude $E_\mathrm{0,i}$ and n_j, $j = \{1,2\}$ is the refractive index of the j-th material. The transmissive wave propagates at an angle of β. Note, the coefficients are complex, i.e. $\left(\frac{E_\mathrm{0,r}}{E_\mathrm{0,i}}\right)_\perp, \left(\frac{E_\mathrm{0,r}}{E_\mathrm{0,i}}\right)_\parallel \in \mathbb{C}$, due to the complex refractive index in an absorbing material. With the parallel $R_\parallel = r_\parallel^2$ and perpendicular $R_\perp = r_\perp^2$ reflectivity, the reflectivity is then given by $R = R_\perp + R_\parallel$.

In addition to the direct absorptance due to the laser fluence, the accumulated heat in the material fosters ablation. In order to account for that in the threshold model, a

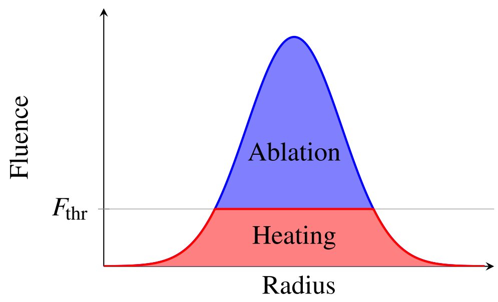

Fig. 2 Separation of the fluence of a Gaussian beam into ablation and heating parts.

temperature-dependent threshold is defined from an energy balance in the material. With the temperature $T := T(\vec{x},t) : \mathbb{R}^3 \times \mathbb{R} \to \mathbb{R}$ and the internal energy density $e : \mathbb{R}^3 \times \mathbb{R} \to \mathbb{R}$ the balance reads

$$\rho e = \rho C_p (T - T_0) + \rho H_{\mathrm{m}} + \rho H_{\mathrm{v}}, \tag{6}$$

where the space and time dependency is dropped for the sake of a shorter notation. The energy in the material is the sum of the inner energy $u = \rho C_p (T - T_0)$, the melting enthalpy H_{m}, and the evaporation enthalpy H_{v}. The internal energy is expressed in terms of the heat capacity at constant pressure C_p and the temperature difference. From the definition of the fluence threshold, we have

$$\rho e(T_{\mathrm{v}}) d_{\mathrm{heat}} = F_{\mathrm{thr}}, \tag{7}$$

which yields, for given threshold fluence, the ablation depth due to stored heat d_{heat}. In case of a preheated material, more of the fluence directly contribute to ablation as it is not needed to heat up the material. Therefore, we can lower the threshold by

$$F_{\mathrm{thr}}(T) = F_{\mathrm{thr}}(T_0) - \rho C_p (T - T_0) d_{\mathrm{heat}}. \tag{8}$$

3.2. Heating the Material

In the previous section, an absorption criterion is described. It states that fluence values greater than a threshold drives the ablation of material. The remaining fluence, which is not converted to ablation, will result in heating of the material (cf. fig. 2). In order to get the temperature field within the sheet metal foil, a heat conduction equation has to be solved, i.e.

$$\begin{aligned} \rho C_p \frac{\partial T}{\partial t} - \nabla\cdot(\lambda \nabla T) &= 0, && \text{in } \Omega \times \mathscr{I} \\ T &= T_0(\vec{x}), && \text{in } \Omega \times \{0\} \\ \vec{q} &= \vec{q}_0(\vec{x},t), && \text{on } \partial\Omega \times \mathscr{I}. \end{aligned} \tag{9}$$

This system is closed with Fourier's law for the heat flux $\vec{q} = -\lambda \nabla T$.

3.3. Evolving the Ablation Front

From the ablation depth d_{abl} and the pulse duration τ_{p}, an ablation velocity can be defined $\vec{v}_{\mathrm{abl}} = (d_{\mathrm{abl}}/\tau_{\mathrm{p}})\vec{n}$ which points in normal direction of the surface. It is assumed here, that the ablation time corresponds to the pulse duration $\tau_{\mathrm{abl}} \simeq \tau_{\mathrm{p}}$. The normal velocity enters a Hamiltonian-Jacobi type equation which is solved for the implicitly defined surface $\phi : \mathbb{R}^3 \times \mathbb{R} \to \mathbb{R}$, i.e.

$$\begin{aligned} \frac{\partial \phi}{\partial t} + H(\nabla\phi) &= 0, && \text{in } \Omega \times \mathscr{I} \\ \phi &= \phi_0(\vec{x}), && \text{in } \Omega \times \{0\} \end{aligned} \tag{10}$$

through the Hamiltonian $H(\nabla\phi) := \vec{v}_{\mathrm{abl}} \cdot \nabla\phi$. Here, ϕ defines the surface implicitly, i.e. $\partial\Omega_t := \{\vec{x} \in \mathbb{R}^3 \mid \phi(x,t) = 0\}$. Additionally, it is a distance function and, therefore, the normal can be expressed in terms of ϕ and the Hamiltonian reads $H(\nabla\phi) := d_{\mathrm{abl}}/\tau_{\mathrm{p}} |\nabla\phi|$. Solving eq. (10) yields a function that describes the evolving surface due to ablation.

4. Numerical Discretization

The models for heating the material, evolving the ablation front, and plastic displacements require a numerical treatment in order to be solved. In the following sequel, the different techniques used for the discretization of these models are described.

4.1. Heating the Material

The heat equation is discretized using an implicit Euler or first order Backward Differentiation Formula (BDF) in time and a Bubnov-Galerkin method for the spatial dimensions. The BDF-1 of eq. (9) reads, after some rearranging,

$$\rho C_p T^{i+1} - \Delta t \nabla\cdot(\lambda \nabla T^{i+1}) = T^i. \tag{11}$$

Herein, the superscript $i+1$ denotes the next time step to be solved for and the superscript i is a previous solution. The time step Δt is computed from a Courant-Friedrichs-Lewy (CFL) condition with CFL number $C \approx 1$, i.e. $\Delta t = C(\Delta x)^2/4$, where Δx denotes the element's shortest edge.

In order to apply the Bubnov-Galerkin method in space, the Hilbert function space H_0^1, which contains functions that are Lebesgue-integrable up to first order derivatives and vanish on the boundary of the domain, is chosen for trial and test functions alike. The temperature is approximated in the discretized Hilbert space by $T(\vec{x},t) \approx \sum_{n=0}^{N}, \tilde{T}_n(t)\theta_n(\vec{x}),\ \theta_n \in H^2_{0,\mathrm{d}}$. Inserting this expression into eq. (11), multiplying by arbitrary, finite test functions $\varphi_m \in H^2_{0,\mathrm{d}},\ m = 0,\ldots,M$, and integrating over the domain Ω yields after integration-by-parts

$$\begin{aligned} &\sum_{n=0}^{N} \int_\Omega \left(\rho C_p \tilde{T}_n^{i+1}\theta_n - \Delta t \lambda \nabla \tilde{T}_n^{i+1}\theta_n\right) \varphi_m \,\mathrm{d}V \\ &\qquad = -\int_{\partial\Omega} \varphi_m \vec{q}_0 \vec{n} \,\mathrm{d}S + \int_\Omega \left(\sum_{n=0}^{N} \tilde{T}_n^i \theta_n\right) \varphi_m \,\mathrm{d}V. \end{aligned} \tag{12}$$

After some rearranging, this can be brought into matrix form

$$\vec{A}\vec{\tilde{T}}^{i+1} = \vec{b}, \tag{13}$$

with the mass matrix $\vec{A} \in \mathbb{R}^{N\times M}$ and load vector $\vec{b} \in \mathbb{R}^M$. The entries of the mass matrix are given by

$$A_{nm} = \int_\Omega \left(\rho C_p \theta_n \varphi_m - \Delta t (\lambda \nabla \theta_n) \nabla \varphi_m\right) \mathrm{d}V \tag{14}$$

and the load vector's entries read

$$b_m = -\int_{\partial\Omega} \varphi_m \vec{q}_0 \cdot \vec{n} \,\mathrm{d}S + \int_\Omega \left(\sum_{n=0}^{N} \tilde{T}_n^i \theta_n\right) \varphi_m \,\mathrm{d}V. \tag{15}$$

The heat flux at the top boundary Γ_{top} is given by the Laser fluence used to heat the material, i.e.

$$F_{\mathrm{heating}} := \begin{cases} F_{\mathrm{L}}, & \text{if } F_{\mathrm{L}} < F_{\mathrm{thr}} \\ F_{\mathrm{thr}}, & \text{otherwise}, \end{cases} \tag{16}$$

integrated over the laser pulse duration

$$\vec{q} = \int_{\tau_0}^{\tau_{\mathrm{end}}} F_{\mathrm{heating}}\, \mathrm{d}t = F_{\mathrm{heating}}\, \tau_{\mathrm{p}}. \tag{17}$$

Herein, the laser pulse, and therefore the laser fluence, is assumed to be a perfect square wave signal. For an exemplary visualization for the splitting of the fluence into ablation and heating parts see fig. 2.

4.2. Evolving the Ablation Front

For the Hamilton-Jacobi equation, a forward Euler in time and Local Lax-Friedrichs (LLF) scheme in space has been implemented as described in the monograph of Osher and Fedkiw [3]. The forward Euler discretization of eq. (10) reads

$$\frac{\phi^{n+1} - \phi^{n}}{\Delta t} + H(\nabla \phi) = 0. \tag{18}$$

The time step Δt is choosen such that the CFL condition holds, i.e.

$$\Delta t \max \left\{ \frac{|H_x|}{\Delta x} + \frac{|H_y|}{\Delta y} + \frac{|H_z|}{\Delta z} \right\} < 1. \tag{19}$$

Herein, $H_i = \vec{v}_{\mathrm{abl}} \phi_i / (|\nabla \phi|)$, $i = \{x, y, z\}$ are the partial derivatives of H.

Then, the space discretization is done on a cartesian grid

$$\frac{\phi^{n+1} - \phi^{n}}{\Delta t} + \hat{H}(\phi_x^-, \phi_x^+, \phi_y^-, \phi_y^+, \phi_z^-, \phi_z^+) = 0. \tag{20}$$

The notation ϕ_i^j, $i = \{x, y, z\}$, $j = \{-, +\}$ denotes first order accurate one-sided partial derivatives wrt. the different coordinates at a grid point.

For a consistent approximation of the Hamiltonian, the LLF scheme is used, i.e.

$$\hat{H} = H\left(\frac{\phi_x^- + \phi_x^+}{2}, \frac{\phi_y^- + \phi_y^+}{2}, \frac{\phi_z^- + \phi_z^+}{2} \right) - \alpha \left(\frac{\phi_x^+ - \phi_x^-}{2} \right) - \beta \left(\frac{\phi_y^+ - \phi_y^-}{2} \right) - \gamma \left(\frac{\phi_z^+ - \phi_z^-}{2} \right), \tag{21}$$

with the dissipation coefficients $\alpha := \max |\vec{v}_{\mathrm{abl}} \phi_x / (|\nabla \phi|)|$ and β, γ accordingly. The coefficients bear no physical meaning but control the error caused by the discretization of the Hamiltonian using a local correction which accounts for the largest front velocity in the direction of the outward pointing normal.

In the LLF scheme, the maximum is evaluated in a neighborhood around the currently evaluated grid point and not for the entire domain. In addition, for the dissipation coefficient associated with the x-coordinate direction, i.e. α, only the value of ϕ_x at the particular grid point is considered. Whereas the values of ϕ_y and ϕ_z are considered within a neighborhood of the current point. The neighborhood of a point $\vec{x}^*$ in this case reads

$$\mathscr{N} := \left\{ \vec{x} \in \mathbb{R}^3 \mid x \in [x_i^*] \times [x_{j-3}^*, x_{j+3}^*] \times [x_{k-3}^*, x_{k+3}^*] \right\}, \tag{22}$$

with the indices i, j, k referring to x-, y-, and z-coordinate entry, respectively. Note, for the coefficients β and γ the neighborhood is choosen accordingly, but with the y-, or z-coordinate fixed, respectively.

Tab. 1 Experimental set-up for the three area ablations and the pyramid.

Description	Value
Repetition rate	$f_{\mathrm{rep}} = 100\,\mathrm{kHz}$
Focal length	$F_\theta = 100\,\mathrm{mm}$
Beam waist (single hole)	$\omega_0 = 8\,\mu\mathrm{m}$
Beam waist (ablation pattern)	$\omega_0 = 16\,\mu\mathrm{m}$
Fluence (pyramid)	$F_{\mathrm{L}} = 0.7\,\mathrm{J/cm^2}$
Fluence (area ablation)	$F_{\mathrm{L}} = 1.4\,\mathrm{J/cm^2}$
Repeats (pyramid)	1
Repeats (area ablation)	$16i,\ i = \{1, 2, 3\}$
Scan velocity (pyramid)	$400\,\mathrm{mm/s}$
Scan velocity (area ablation)	$400\,\mathrm{mm/s}$

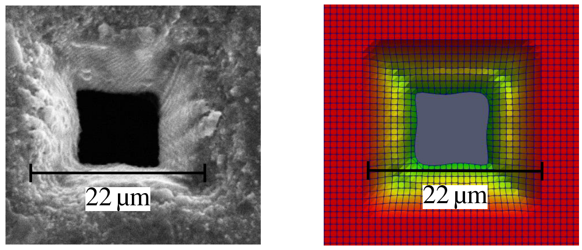

Fig. 3 Single hole ablated with $p = (-1, 1)^T$ polarized light (experiment on the left and simulation on the right).

5. Experiments

The ablation model has been validated against two experiments. A single bore hole and a complex ablation pattern. In both experiments the material stainless steel (DIN 1.4301) is processed. The experiments have been conducted on a custom multi-beam scanner mounted on a TruMicro5280 femto. The scanner has been developed in-house at the Fraunhofer Institute for Laser Technology. The TruMicro5280 is capable of producing a pulse duration of $\tau = 900\,\mathrm{fs}$ and features a laser with maximum energy per pulse of $E_{\mathrm{p}} = 125\,\mu\mathrm{J}$, a wave length of $\lambda = 515\,\mathrm{nm}$, and a maximum power of $P_{\mathrm{L}} = 75\,\mathrm{W}$. Structuring the single square hole has been performed using a polarization of $\vec{p} = (-1, 1)^T$ while for the other experiment a circular polarized laser beam has been used. The remaining process parameters are listed in table 1.

In fig. 3, the result of structuring a square is displayed. Both, the experiment and the simulation, show a pillow shaped hole with sharp corners at the upper left and lower right ones and round corners at the upper right and lower left ones.

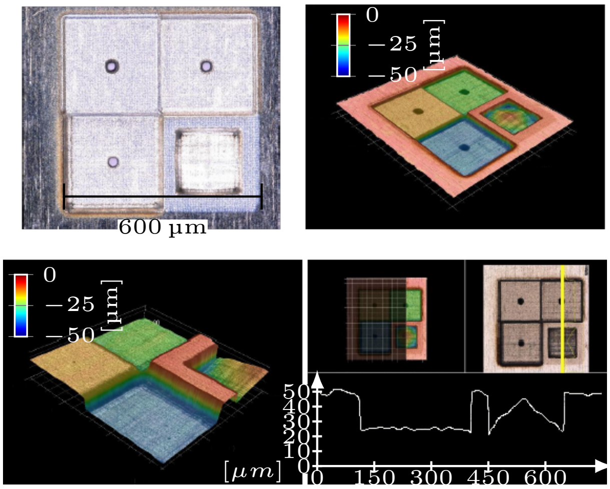

Fig. 4 Complex ablation pattern structured with circularly polarized light.

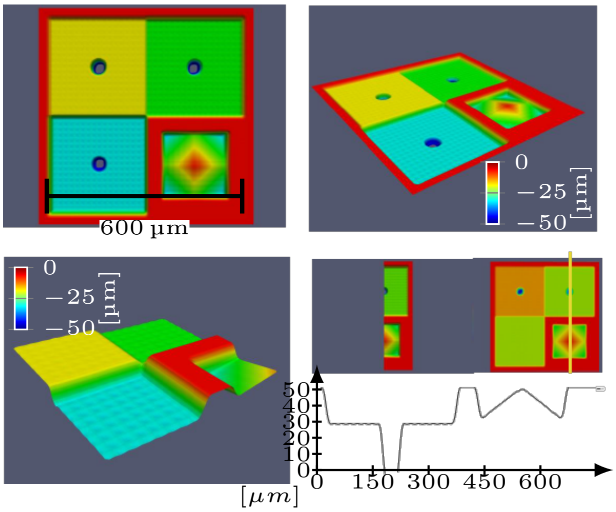

Fig. 5 Simulation result of the complex ablation pattern.

The complex ablation pattern consists of 3 areas which are repeatedly ablated: 16, 32, and 48 times, respectively, and a pyramid. Figure 4 is composed of four different views of this experiment: 1. a birds-eye few on the upper left, 2. an angled few with ablation colorcoded from red (shallow) to blue (deep) on the upper right, 3. a zoomed-in look to the mid-section of the same on the lower left, and 4. a combined view which also shows a cross section highlighted in yellow. The respective simulation result is shown in a similar picture matrix (cf. fig. 5). Again, the ablation depth ranges from red (no or shallow) to blue (deep).

6. Discussion

The simulation results qualitatively match the experiments very well. In the ablated square hole case, both, the pillow shape and the corners, are visible in the simulation.

The pillow shape in fig. 3 can be explained with the acceleration and deacceleration of the scanner, respectively. In the corners, the scan speed is slower than in the middle of the sides and more fluence is absorbed by the material. This causes more ablation in the corners compared to the sides of the square pattern. In other words, more material is left intact on the sides compared to the corners.

The sharp and round corners on the other hand result from the polarization of the laser beam. In fig. 3, the polarization vector points from the lower right to the upper left corner. This translates to an orthogonal polarization vector wrt. the surface at these points and a parallel polarization vector wrt. the surface at the other points. Because the absorbed fluence depends on the polarization as shown in eqs. (2), (4) and (5), more fluence is brought into the material where the polarization vector and the surface are perpendicular to each other. This sharpens the upper left and lower right corners and smoothes out the other two.

For one side, from corner to corner, there is an acceleration phase followed by a constant feed rate followed by a deacceleration phase. Since the repitition rate is constant, the pulses are spatially closer together and therefore more fluence is brought into the material which in turn causes more ablation.

The simulation results for the complex structure show the different depths for 16, 32, and 48 repeats and even the cross section through the pyramid is in perfect agreement with the experiment.

7. Conclusion and Outlook

In this treatise, the ablation of material with a multi-beam scanner with applications to FMM production has been investigated. A mathematical model, composed of three submodels (1. a fluence threshold model, 2. a level-set method which describes the surface evolution, and 3. a heat conduction problem), has been developed. The transport equation was discretized using a forward Euler method in time and a finite-difference scheme in space. In addition, the LLF scheme was used to handle the Hamiltonian flow. For the heat conduction problem the first order BDF procedure was utilized for the time dimension and a Bubnov-Galerkin scheme for the spatial dimensions.

The implementation of the mathematical model is capable of simulating the relevant processes on a micro-scale and reproduces the results seen in the conducted experiments well. The shape of a bore hole could be explained with the polarization of the light and the acceleration of the scanner.

The model has not been studied for very fast repetition rates, such that heat diffusion does not occur inbetween consecutive pulses, i.e. $f_{\text{rep}} \geq 1/\tau_{\text{diff}}$. In this case, the authors expect that the energy absorbed by the electrons and at a later time transferred into the phonon system affects the ablation after the pulses have been deposited into the material and, therefore, this effect would have to be accounted for.

It is not feasible to simulate whole build parts with the micro-scale model due to the computational demands. Therefore, a multi-scale model has already been developed. The description of this model will be part of a companion publication. In order to use the simulation as a digital tool for active process development in the future, a fine-tuning of the simulation to the corresponding USP processing machine is necessary. This requires an experimental procedure in which the material properties for the USP absorption model can be calibrated independently of each other.

Acknowledgement

Funded by the Deutsche Forschungsgemeinschaft (DFG, German Research Foundation) under Germany's Excellence Strategy — EXC-2023 Internet of Production — 390621612.

References

[1] O. Hofmann, O. Chemerenko, J. Finger, S. Eifel, J. Stollenwerk, and P. Loosen: Proc. CIRP, 94, (2020) 2212-8271.

[2] S. Eifel: "Effizienz- und Qualitätssteigerung bei der Lasermikrobearbeitung mit UKP-Lasern durch neue optische Systemtechnik", (Apprimus, Aachen, 2015) p.167.

[3] S. Osher and R. P. Fedkiw: "Level Set Methods and Dynamic Implicit Surfaces", (Springer, New York, 2003) p.273.

[4] B. Neuenschwander, B. Jäggi, M. Schmid, and G. Hennig: Phys. Proc., 56, (2014) 18753892.

[5] B. Jäggi, B. Neuenschwander, M. Schmid, M. Muralt, J. Zuercher, and U. Hunziker: Phys. Proc., 12, (2011) 18753892.

[6] B. Lauer, B. Jäggi, and B. Neuenschwander: Phys. Proc., 56, (2014) 18753892.

[7] B. Neuenschwander, B. Jaeggi, and M. Schmid: Phys. Proc., 41, (2013) 18753892.

[8] M. Born and E. Wolf: "Principles of Optics: Electromagnetic Theory of Propagation, Interference, and Diffraction of Light", (Cambridge University Press, Cambridge, 2019) p.852.

(Received: June 24, 2021, Accepted: October 20, 2021)